Research Article | Vol. 26, No. 23 | 12 Nov 2018 | OPTICS EXPRESS 30347
Optics EXPRESS

Dual-polarized highly sensitive plasmonic sensor in the visible to near-IR spectrum

MD. SAIFUL ISLAM,[1,2,*] JAKEYA SULTANA,[1] AHMMED. A. RIFAT,[3] RAJIB AHMED,[4] ALEX DINOVITSER,[1] BRIAN W.-H. NG,[1] HEIKE EBENDORFF-HEIDEPRIEM,[2] AND DEREK ABBOTT[1]

[1] *National T-Ray facility, School of Electrical & Electronic Engineering, University of Adelaide, SA 5005, Australia.*
[2] *Institute of Photonics & Advance Sensing (IPAS), University of Adelaide, SA 5005, Australia.*
[3] *Nonlinear Physics Centre, Research School of Physics and Engineering, Australian National University, Canberra, Acton 2601, Australia.*
[4] *Bio-Acoustic MEMS in Medicine (BAMM) Laboratory, School of Medicine, Stanford University, Palo Alto, CA 94304, USA.*
[*] *mdsaiful.islam@adelaide.edu.au*

Abstract: We propose and numerically characterize the optical characteristics of a novel photonic crystal fiber (PCF) based surface plasmon resonance (SPR) sensor in the visible to near infrared (500–2000 nm) region for refractive index (RI) sensing. The finite element method (FEM) is used to design and study the influence of different geometric parameters on the sensing performance of the sensor. The chemically stable plasmonic material gold (Au) is used to produce excitation between the core and plasmonic mode. On a pure silica (SiO_2) substrate, a rectangular structured core is used to facilitate the coupling strength between the core and the surface plasmon polariton (SPP) mode and thus improves the sensing performance. By tuning the geometric parameters, simulation results show a maximum wavelength sensitivity of 58000 nm/RIU (Refractive Index Unit) for the x polarization and 62000 nm/RIU for the y polarization for analyte refractive indices ranging from 1.33 to 1.43. Moreover, we characterize the amplitude sensitivity of the sensor that shows a maximum sensitivity of 1415 RIU^{-1} and 1293 RIU^{-1} for the x and y polarizations, respectively. To our knowledge, this is the highest sensitivity for an SPR in published literature, and facilitates future development of sensors for accurate and precise analyte measurement. The sensor also attains a maximum figure of merit (FOM) of 1140 and fine RI resolution of 1.6×10^{-6}. Owing to strong coupling strength, high sensitivity, high FOM and improved sensing resolution, the proposed sensor is suited for real-time, inexpensive and accurate detection of biomedical and biological analytes, biomolecules, and organic chemicals.

1. Introduction

In the last few decades, surface plasmon resonance (SPR) sensing technology has reached a unique place because of its ability to achieve high sensitivity and reliability [1]. Note that SPR is an optical phenomenon that can be defined as the collective oscillation of free electrons on the interface between the metal and dielectric. Resonance occurs when the wavelength of photons of the incoming electromagnetic wave matches with the wavelength of surface electrons. At resonance condition, a sharp loss peak is obtained for a particular analyte of RI and an unknown analyte with different RI can be detected by observing the variation of loss peak and corresponding resonance wavelength. A tiny change in environmental RI potentially shifts the resonance wavelengths, and offers potential application in bio-sensing for label-free and real-time detection of the kinetics of various biological processes [2]. The other significant application areas of SPR sensors range from medical diagnostics, medical testing, bio-molecular analyte detection, antigen-antibody interactions, environmental monitoring for security and food safety [3–5]. Moreover, SPR technology is considered advantageous because of its effectiveness

#332374 https://doi.org/10.1364/OE.26.030347
Journal © 2018 Received 25 May 2018; revised 28 Jun 2018; accepted 3 Jul 2018; published 5 Nov 2018

Optics EXPRESS

and precision in sensing, real-time and label-free detection, and convenient operation.

The conventional SPR sensing technology is based on the mechanism of Kretschmann and Reathers exploiting attenuated total reflection (ATR) [6]. It is also known as prism based SPR where the incident light required to be launched at a particular angle. Prism based SPR sensors have been widely used since they were invented. However, they require many optical and mechanical (moving) components that make them bulky and incompatible for remote sensing [1, 7–9]. Miniaturization of sensing devices based on optical fiber can overcome the drawbacks faced by prism based sensors and offers advantages such as remote-sensing, simple and flexible sensor design, continuous analysis and *in situ* monitoring [10, 11]. Moreover, conventional optical fibers are immune to electromagnetic interference, mechanically stable and experience low confinement loss in the visible range. However, there is insufficient freedom for tuning the design parameters since there are relatively few parameters to change [9].

In recent years, photonic crystal fiber (PCF) based SPR sensors have gained significant attention owing to their novel structural characteristics and optical properties such as single mode guidance of light, design flexibility and controllable birefringence [15–17]. Note that a PCF is compact and light weight, which permits miniaturization of the sensors, making them attractive for remote sensing applications [10, 12, 13]. In a PCF the plasmonic metal layer can be coated inside of the air holes or outside the fiber surface. Moreover, incident light can simply be launched at one end of the PCF where the response can be observed from the other end. In addition, the PCF design can be optimized to achieve strong coupling between the core mode and SPP mode that consequently improves sensing performance [14, 15].

The plasmonic materials gold (Au) and silver (Ag) are the most commonly used active metals for coating the walls of a PCF-SPR sensor. Gold is chemically stable, bio-compatible, and gives rise to a larger shift of resonance wavelength. On the other hand, silver gives rise to a sharper resonance peak compared to gold. However when placed in a humid environment the silver becomes oxidized and this reduces the analyte detection accuracy [14]. For this reason, much theoretical as well as experimental work has been carried out using gold as the plasmonic material [18, 29].

An SPR based PCF sensor involves two types of sensing mechanism. One is internal sensing and the other is external sensing. The sensing is called internal when the analyte selectively fills the air holes, whereas when the analyte is placed at the surface of a PCF the sensing mechanism is called external sensing. In recent years, several sensors using an internal sensing mechanism have been reported in the literature [17–24]. Among them, the most recent work reported by Rifat *et al.* [24] proposed a gold coated sensor and obtained a maximum wavelength and amplitude sensitivity of 11000 nm/RIU and 1420 RIU^{-1} respectively. However, the internal sensing mechanism is not suitable for real-time and distributed sensing applications. This is due to the need to change the analyte during measurement and the emptying and refilling of selected air holes are difficult and time consuming [25]. Moreover, fabrication of an internally metal coated PCF-SPR sensor is quite difficult due to the requirements to coat or infiltrate analytes onto the tiny air hole surface [29]. The fibers also experience a large propagation loss as the plasmonic metal layers are selectively placed surrounding the core.

Note that PCFs with a D-shaped structure provided a solution and a number of D-shaped PCF-SPR sensors have been reported [6, 25–27, 29–32]. Among the reported D-shaped structures, Wang *et al.* in 2016 reported a maximum wavelength sensitivity of 12450 nm/RIU within the RI range of 1.345–1.410 [27]. Without mentioning the amplitude sensitivity they obtained a sensor resolution of 8.03×10^{-6}. Moreover, from the loss peak curve of ref. [27] we can see that a sharp loss peak is obtained for large value of analyte RI while the peak at low RI is broadening and that may cause mis-detection of analytes. In the following year Huang *et al.* proposed an indium tin-oxide based D-shaped sensor structure and obtained a maximum wavelength sensitivity of 6000 nm/RIU and a low amplitude sensitivity of 148 RIU^{-1} in the RI range of 1.28–1.34 [28].

Optics EXPRESS

However, a maximum wavelength and amplitude sensitivity of 46000 nm/RIU and 1086 RIU^{-1} was obtained with an analyte RI of 1.33 to 1.43 [29]. Although cleaning a D-shaped structure is convenient for refilling with analyte, the standard polishing and etching of particular parts are challenging in practice [33, 34].

Considering the limitations faced by the internal sensing approach as well as D-shaped structure of the external sensing approach, PCFs with a different external sensing mechanism were reported where the analyte channel is in contact with the outer surface of the PCF [10, 35–39]. Among the PCFs proposed with this external sensing approach, Liu *et al.* recently obtained a maximum wavelength sensitivity of 15180 nm/RIU within the analyte RI of 1.40 to 1.43 [39]. Therefore, the literature discussed above indicates that there is sufficient scope for new SPR sensor designs with improved sensing performance.

In this manuscript, utilizing an external sensing approach we propose a novel gold coated PCF-SPR sensor to operate in the visible to near-infrared region. Note that at near-infrared the penetration depth of the evanescent field is high resulting in improved detection of analytes, and low-cost laser sources are commercially available [40]. We introduce a rectangular shaped core structure that facilitates coupling, which further improves the sensing performance. The aim is to obtain high detection accuracy in a sensor that can be readily fabricated. For ease of fabrication and practical utilization of the sensor, the metal coating is applied to the outer surface of the fiber, with the plasmonic surface in direct contact with the analyte. Various geometric parameters such as pitch distance, air hole diameter, core geometry, analyte channel thickness, metallic channel thickness and PML thickness are optimized for obtaining the desired performance.

2. Design and theoretical modelling of the proposed PCF-SPR sensor

The modelling and performance evaluation of the proposed PCF-SPR sensor are carried out using commercially available finite element method (FEM) based software COMSOL *v*5.3. The schematic of the proposed sensor is shown in Fig. 1 (a). *Physics-controlled mesh* sequence with *extremely fine* element size is used to achieve maximum accuracy in simulation. In a silica (SiO_2) substrate, a circular air hole based circular shaped cladding is proposed.

Different diameters of air holes (d, d_1 and d_2) are used to shape the cladding that has significant effect on confinement loss and light propagation through fiber that is discussed in the later section of this manuscript. Here, air holes with diameter d are used to couple light from core mode to interact with the plasmonic mode so that a strong interaction between core and plasmonic mode can be created. The air holes with diameter d_1 confine light from the core mode, to the plasmonic mode aside from the outer holes. In this way the power density in the core mode is increased to interact strongly throgh the specified area of plasmonic mode. In addition, the air holes with diameter d_2 are used to reduce the confinement loss. A rectangular air hole is used at the center of the core to create asymmetry between the polarization modes that in turn helps improving the sensing performance [41]. Addition of rectangular air hole in the core help the core power to strongly couple with the surface that also help creating birefringence effect on the sensor. Moreover, we use four channels of light penetration from the core mode to the plasmonic mode to improve the performance of the sensor. Note that an artificial boundary condition named perfectly matched layer (PML) is added at the outer surface of the computational region that potentially absorbs radiation energy. We optimize the air hole diameters (d, d_1 and d_2), rectangle width (W) and height (H), pitch distances (Λ, Λ_1 and Λ_2), gold (t_g), analyte (t_a) and PML (t_p) thickness to determine the optimal design conditions. After careful investigation we choose $H = 0.5$ μm, $W = 0.15$ μm, $\Lambda = 1.8$ μm, $\Lambda_1 = 1.6$ μm, $\Lambda_2 = 1.24$ μm, $d = 1.35$ μm, $d_1 = 1.20$ μm, $d_2 = 0.18$ μm, $t_g = 30$ nm, $t_a = 0.9$ μm, and $t_p = 1.0$ μm as optimal. Optimization of these parameters is briefly discussed in Section 3. In the designed sensor, the analyte is in contact with the outer surface that can be cleaned for reuse with different analytes—this removes the difficulties with internal sensing as well as external sensing with a D-shaped structure that

Optics EXPRESS

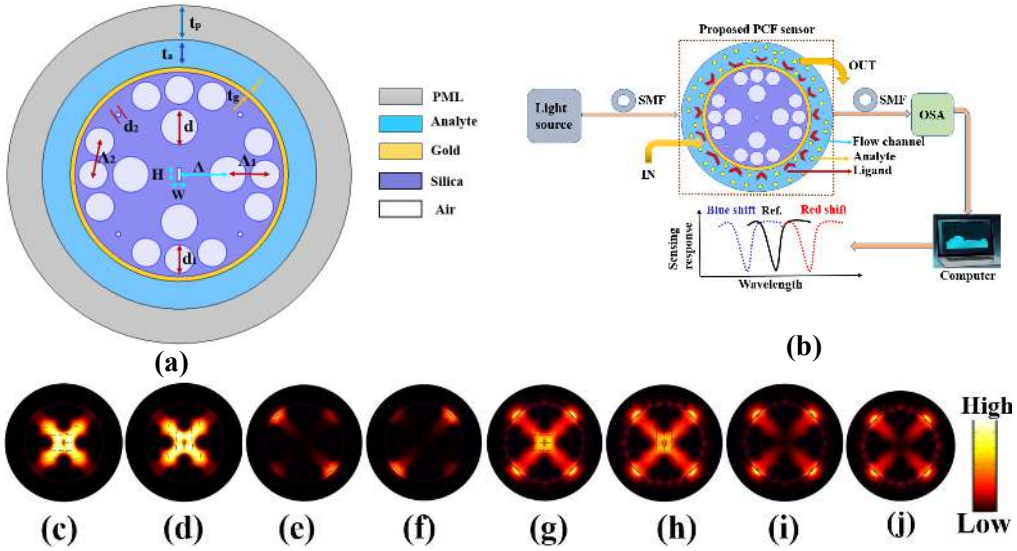

Fig. 1. Schematic of the cross section (a), general set-up for practical sensing (b), core mode (c-d) and SPP mode (e-f) for analyte RI 1.33 and for analyte RI 1.42 (g-j) respectively at $H = 0.5\ \mu$m, $W = 0.15\ \mu$m, $\Lambda = 1.8\ \mu$m, $\Lambda_1 = 1.6\ \mu$m, $\Lambda_2 = 1.24\ \mu$m, $d = 1.35\ \mu$m, $d_1 = 1.20\ \mu$m, $d_2 = 0.18\ \mu$m, $t_g = 30$ nm, $t_a = 0.9\ \mu$m, and $t_p = 1.0\ \mu$m.

needs careful surface polishing [29, 32].

The material dispersion of pure silica can be calculated using the Sellmeier Eq. [31, 43],

$$n = \sqrt{1 + \frac{0.692\lambda^2}{\lambda^2 - 0.0047} + \frac{0.408\lambda^2}{\lambda^2 - 0.014} + \frac{0.897\lambda^2}{\lambda^2 - 97.934}} \tag{1}$$

where n represents the RI of silica and λ stands for the wavelength of light. Note that, Eq. (1) is valid for the wavelength region of 0.37 to 2.2 μm [31, 43].

The material dispersion of gold can be determined from the Drude-Lorentz model [42, 44],

$$\varepsilon_m = \varepsilon_\infty - \frac{\omega_D^2}{\omega(\omega + j\gamma_D)} + \frac{\Delta_\varepsilon . \Omega_L^2}{(\omega^2 - \Omega_L^2) - j\Gamma_L\omega} \tag{2}$$

where $\varepsilon_\infty = 5.9673$ is the permittivity of gold, $\Delta_\varepsilon = 1.09$ is the weighting vector, ω is the angular frequency of the guided light, ω_D and γ_D are defined as the plasma frequency and damping frequency, where $\omega_D/2\pi = 2113.6$ THz, and $\gamma_D/2\pi = 15.92$ THz. Moreover, Ω_L and Γ_L indicate the frequency and spectral width of the Lorentz oscillator where $\Omega_L/2\pi = 650.07$ THz and $\Gamma_L/2\pi = 104.86$ THz.

Confinement loss of the proposed sensor can be calculated by using the imaginary part of the complex RI by using both the following Eq. [29],

$$\alpha_{\text{loss}} = 8.686 \times \frac{2\pi}{\lambda} \times \text{Im}(\text{n}_{\text{eff}}) \times 10^4,\ \text{dB/cm} \tag{3}$$

where, α_{loss} stands for the confinement loss, λ specifies the operating wavelength in micron scale, and $\text{Im}(\text{n}_{\text{eff}})$ represents the imaginary part of the complex RI.

Note that the performance evaluation of the proposed sensor is carried out using both wavelength interrogation (WI) and amplitude interrogation (AI) method. According to WI method the

wavelength sensitivity can be calculated according to the following Eq. [32],

$$S_W(\lambda) = \frac{\Delta\lambda_{\text{peak}}}{\Delta n_{\text{a}}} \tag{4}$$

where, $\Delta\lambda_{\text{peak}}$ and Δn_{a} denotes the shift in resonance peaks and analyte RI respectively.

It can be mentioned that the AI method is less complex since in this method the output beam is analyzed at a particular wavelength where spectral manipulation is not needed [45]. Therefore, AI method only requires a power meter and however, AI is very sensitive to disturbances. Usually ratiometric approaches are used, where the sensitive intensity is compared to the intensity of a reference peak which is not sensitive to the parameter to be measured and thus any fluctuation in laser power, coupling, etc is removed via normalising to the reference peak intensity. If the input power launched into the fiber is P_0, the detected power at the output can be found by the following expression

$$P(L, \lambda, n_{\text{a}}) = P_0 e^{-\alpha(\lambda, n_{\text{a}})L} \tag{5}$$

where, $\alpha(\lambda, n_a)$ is the attenuation constant and can be defined by Eq. (3), L indicate the length of the sensor that can be defined by

$$L = \frac{1}{\alpha(\lambda, n_a)}. \tag{6}$$

The amplitude sensitivity of the sensor can be calculated according to the following Eq. [45],

$$S_A(\lambda) = -\frac{1}{\alpha(\lambda, n_{\text{a}})} \frac{\delta\alpha(\lambda, n_{\text{a}})}{\delta n_{\text{a}}} \tag{7}$$

where, the difference between two loss spectra due to a small change of analyte RI is denoted by $\delta\alpha(\lambda, n_{\text{a}})$, and δn_{a} indicates the change in analyte RI.

Preserving the polarization state is also important in consideration of sensing applications; eliminating the polarization mode dispersion (PMD), as well as stabilizing the operation of optical devices. Birefringence determines the polarization states of a fiber that is defined as the RI difference between the polarization modes. It can be calculated by the following Eq. [46,47],

$$B = |n_x - n_y| \tag{8}$$

here, B indicates the birefringence, n_x represents the effective mode index in the x-polarization and n_y represents the effective mode index in the y-polarization.

Sensor resolution is also an important parameter that determines the degree of detection with analyte RI variation. The resolution of a sensor can be determined by the following Eq. [48],

$$R = \frac{\Delta n_{\text{a}} \Delta\lambda_{\text{min}}}{\Delta\lambda_{\text{peak}}} \tag{9}$$

where, R represents the sensor resolution, Δn_{a} represents the variation of analyte RI, $\Delta\lambda_{\text{min}}$ defines the minimum wavelength resolution, and $\Delta\lambda_{\text{peak}}$ determines the difference in resonance peak shift.

The fabrication of the proposed sensor is straightforward. The differently sized circular shaped air holes can be realized using the standard stack-and-draw method [49,50]. In 2014, Mahdiraji *et al.* [49] and Knight *et al.* [50] utilized the stack-and-draw method to make different circular shaped air holes. Moreover, the rectangular shaped air hole can be fabricated using an extrusion technique [51,52] and 3D printing technology [53]. Note that, Atakaramians *et al.* [51,52] made the rectangular shaped air holes utilizing the extrusion technique. There are several methods such as chemical vapor deposition (CVD), high-pressure microfluidic chemical deposition and

Optics EXPRESS

wheel polishing for obtaining a thin gold layer at the outer surface of the sensor [18, 30, 54–57]. Therefore, the proposed sensor is manufacturable with available fabrication technologies.

A general set-up for practical realization of the sensor is shown in Fig. 1(b). A wide-band or super-continuum light source can be used to launch light into the single mode fiber (SMF). A splicing technique can be used then to couple the SMF with the proposed sensor. An analyte flow channel at the outer layer facilitates the IN and OUT of liquid analyte. The IN and OUT of analytes can be maintained by using a pump. Note that due to the interaction of ligand and analyte, the effective index of the SPP mode is expected to be changed resulting in red or blue shift of the signal. The optical spectrum analyzer can be used to measure the transmitted light through another SMF. Finally the computer can be used to observe and analyze the output spectrum.

3. Investigation of sensor performance by optimizing different optical parameters

The evanescent field produced by the light propagating through the core is the key phenomenon of a PCF-SPR sensor. The evanescent field excite the electrons of the metal surface that result in a surface plasmon wave. As the proposed sensor experiences birefringence due to its asymmetrical structure, we investigate the sensing performance for both polarizations. As an initial step we characterize the evanescent field distribution that indicates strong coupling between the core and SPP mode for both polarization modes as shown in Fig. 1(c)-(j). At resonance wavelength Fig. 1(c)-(j) shows the field distribution for n_a = 1.33 and n_a = 1.42 respectively which shows that for n_a = 1.42 the mode fields are more strongly coupled than n_a = 1.33. These results strong detection of analyte with RI higher than n_a = 1.33.

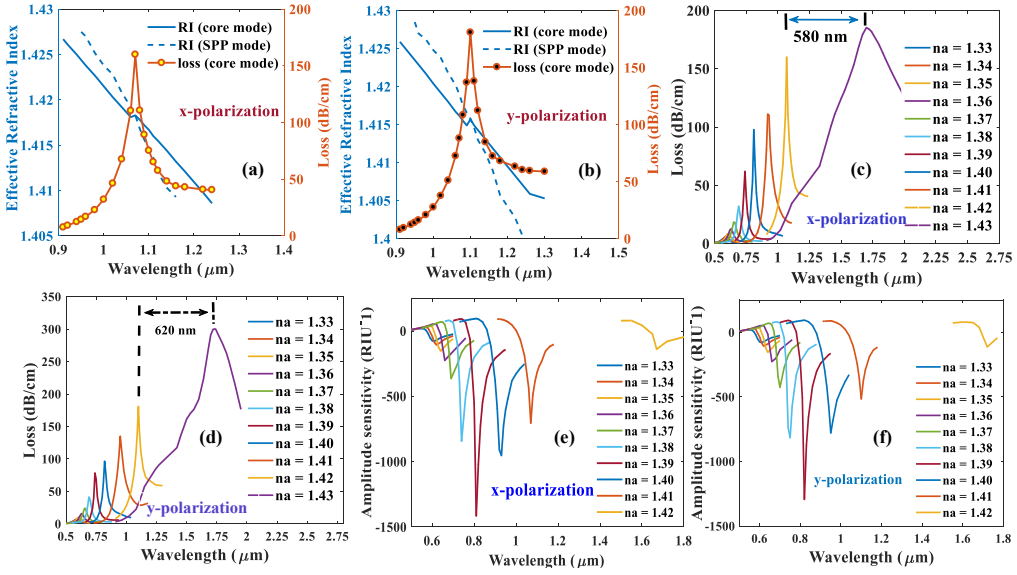

Fig. 2. Dispersion relation of fundamental core mode, SPP mode, and loss spectra of n_a = 1.42 (a-b), confinement loss (c-d) and amplitude sensitivity (e-f) for an analyte RI variation from 1.33 to 1.43 and for *x* and *y*-polarization respectively.

The dispersion profile for fundamental core mode, plasmonic mode and confinement loss as a function of wavelength for both *x* and *y* polarization is shown in Fig. 2 (a-b). It indicates that at the RI matching point of core mode and SPP mode a sharp loss peak is obtained, and sharp loss peak is suitable for efficient and easy detection of analytes [29]. It can be seen from Fig. 2 (a-b) that, for an analyte RI of n_a = 1.42 and *x* polarization the resonance occurred at a wavelength

of 1.07 μm whereas for the y polarization the resonance point shifted to 1.10 μm. This clearly indicates a significant amount of birefringence in this PCF design resulting in strong coupling to one of the two possible orientations. The polarization property of a fiber sensor improves the sensing performance [29, 47].

The characteristics of confinement loss for both the polarizations at an analyte RI variation from 1.33 to 1.43 is shown in Fig. 2 (c-d). Note that, performance measurement of the sensor is carried out using the confinement loss characteristics of different analytes. Figure 2 (c-d) indicate that increase of analyte RI shifts the resonance peak towards longer wavelengths. Note that with a tiny change of analyte RI, the RI of plasmonic mode also changes resulting in a changed phase matching point. During the performance analysis we choose RI from 1.33 to 1.43. This is because the RI of biochemical interactions goes from 1.33 to 1.35 however the range 1.33 to 1.43 is considered based on practical bio-chemical and chemical sensing [60, 61]. It is observed that the resonance peak shift increases with the increase of analyte RI resulting in high sensitivity for larger RI. Note that the proposed sensor shows similar loss characteristics to previously reported [32] highly sensitive sensors. Moreover, from Fig. 2 (c-d) we can see that a maximum resonance wavelength shift of 580 nm and 620 nm is obtained between the analyte RI of 1.42 and 1.43 for the x and y polarization mode respectively. Therefore, a maximum wavelength sensitivity of 58000 nm/RIU and 62000 nm/RIU is obtained at 1.42. To our knowledge, this is the highest wavelength sensitivity reported by a PCF-SPR sensor.

The performance evaluation of the sensor is also carried out using the amplitude interrogation method that calculates amplitude sensitivity. The obtained amplitude sensitivity at both x and y polarization mode is shown in Fig. 2 (e-f). It can be seen that x polarization shows better amplitude sensitivity than y polarization as sharper loss peak is obtained at x than y polarization. The maximum amplitude sensitivity obtained for the x polarization is 1415 RIU^{-1} whereas for the y polarization the sensitivity is 1293 RIU^{-1}.

Note that, to evaluate the overall performance of a sensor, the FOM is defined as the ratio of sensitivity to full width at half minima (FWHM) [32, 58, 59]. In general, to realize a high performance sensor the FOM should be as high as possible that can be obtained when the sensitivity increases and FWHM decreases. The obtained FOM for different analyte is shown in Table 3. We can see that, a maximum FOM of 1140 and 958 is obtained for the x and y polarization respectively that also an indication of improved performance of the proposed sensor over the prior reported [6, 10, 17–26, 29–39] sensors.

For different variation of analyte RI Table 3 shows the characteristics comparison of the proposed sensor for both x and y polarization at optimal design conditions. It indicates that maximum amplitude sensitivity of 1415 RIU^{-1} is obtained at x polarization mode, this is due to the sharper loss characteristics of x polarization than y polarization (see Fig. 2 (c-d)). Moreover, we can see that the maximum amplitude sensitivity is obtained at an analyte RI of 1.39 and it decreases with further increase or decrease of RI from 1.39 (see Fig. 2 (e-f)). This is because of the sharper loss peak obtained between the RI of 1.39 to 1.40 whereas the loss peak broadens for other RI of analytes.

3.1. Effect of different core structures on the sensing performance

The effect of different core structures on the sensing performance of the proposed sensor is investigated. We used different core structure such as rectangular, circular and solid core and analyzed their performance to choose the best one. It is worthwhile to note that there is no particular reason but we randomly choose the RI 1.41 and 1.42 as a reference to observe the characteristics of the sensor at different geometric parameter variations. Thus, by tuning different geometric parameters, further investigation of the sensor is done using analyte RI of 1.41 and 1.42 as reference.

Table 1. Analysis of sensing performance in terms of amplitude sensitivity and wavelength sensitivity with different variation of analyte RI.

Analyte	Peak wavelength (nm)		Amplitude sensitivity (RIU^{-1})		Wavelength sensitivity (nm/RIU)		Figure of Merit (FOM)	
RI	*x*-pol	*y*-pol	*x*-pol	*y*-pol	*x*-pol	*y*-pol	*x*-pol	*y*-pol
1.33	580	580	76	78	1000	1000	14	13
1.34	590	590	105	106	2000	2000	31	30
1.35	610	610	152	153	2000	2000	34	34
1.36	630	630	224	226	2000	3000	37	55
1.37	650	660	363	425	4000	3000	76	60
1.38	690	690	843	816	5000	5000	116	117
1.39	740	740	1415	1293	7000	8000	215	243
1.40	810	820	952	779	11000	13000	357	310
1.41	920	950	704	515	15000	15000	229	197
1.42	1070	1100	139	112	58000	62000	1140	958
1.43	1650	1720	N/A	N/A	N/A	N/A	N/A	N/A

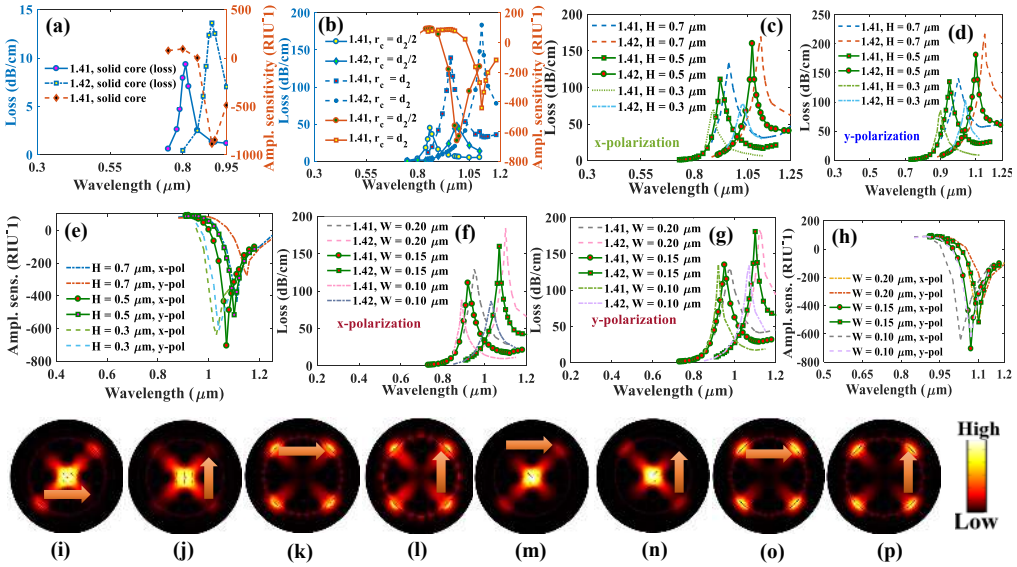

Fig. 3. Performance analysis with (a) solid core, (b) circular shaped core, (c-d) confinement loss and (e) amplitude sensitivity with different H of rectangular core, (f-g) confinement loss and (h) amplitude sensitivity with different W, and electromagnetic field distribution with (i-j) core mode and (k-l) SPP mode having circular shaped air hole in the core and (m-n) core mode and (o-p) SPP mode having solid core.

3.1.1. Performance with solid core

The performance of the sensor with solid core is investigated, with the loss and sensitivity shown in Fig. 3 (a). It shows that solid core experience negligible confinement loss with amplitude and wavelength sensitivity of 886 RIU^{-1} and 10000 nm/RIU respectively for an analyte RI of n_a = 1.41.

3.1.2. Performance with circular shaped air hole in the core

The effect of circular shaped air hole in the core on the sensing performance of the PCF-SPR sensor is also investigated, as shown in Fig. 3 (b). It indicates that use of circular shaped air hole in the core instead of the solid core increases the confinement loss however that also comes with a lower amplitude sensitivity (660 RIU^{-1}) with same wavelength sensitivity.

3.1.3. Performance with rectangular shaped air hole in the core

The performance analysis of the core with rectangular shaped air hole is carried out by varying the height (H) and width (W). For different values of (H) and (W) the characteristics are shown in Fig. 3 (c-h).

From Fig. 3 (c-d) it can be observed that increasing the rectangular height increases the confinement loss by increasing coupling from the core mode to the SPP mode. However, that also reduces the amplitude sensitivity that can be observed from Fig. 3 (e). We can see that as H increases the loss peak also broadens causing a reduction in amplitude sensitivity. Therefore, we cannot consider $H = 0.7$ μm as an optimum height of the rectangular core. Moreover, for $H = 0.3$ μm we can see that the confinement loss decreases and amplitude sensitivity increases significantly as compared to $H = 0.7$ μm. However this also broadens the loss peak and reduces the birefringence therefore we also cannot consider $H = 0.3$ μm as optimum. Note that the broadened characteristic of the loss peak is not suitable for efficient and accurate detection as it decreases the signal to noise ratio that may give rise to a false positive response [29]. For $H = 0.5$ μm it can be observed that a sharp loss peak associated with a highest amplitude sensitivity is obtained for both of the polarization modes. Moreover the obtained wavelength sensitivity at $H = 0.5$ μm is higher (15000 nm/RIU) than $H = 0.3$ μm (14000 nm/RIU). Thus considering all of the above facts we choose $H = 0.5$ μm as optimum height of the rectangular shaped air hole in the core.

In order to optimize the width (W) of the rectangular core we varied W to observed the confinement loss and sensitivity performances that illustrated in Fig. 3 (f-h). With $W = 0.10$ μm, a minimum loss and high amplitude sensitivity is observed, however that also results in a broadened loss peak. We can observe a comparatively sharper loss peak for $W = 0.15$ μm and $W = 0.20$ μm, however the larger width also results in a lower sensitivity. Thus, considering the amplitude sensitivity and confinement loss we choose $W = 0.15$ μm as the optimum width of the rectangular core.

The electric field distribution due to the solid core and core with circular shaped air hole is shown in Fig. 3 (i-p), it indicates that at resonance wavelength the coupling of core mode and SPP mode is weaker than that obtained for rectangular core as shown in Fig. 1 (c-j). Therefore, we obtain better sensing performance by using rectangular shaped air hole in the core than using solid and circular shaped air hole. Therefore, observing the obtained characteristics and analyzing the sensing performances we decide to consider the rectangular shaped structure in the core of the proposed sensor.

The birefringence effect of the sensor using rectangular, circular and solid core is shown and observed from Fig. 4 (a). It indicates that the birefringence effect of a rectangular shaped core is significant as it can create more asymmetry between the polarization modes whereas the circular and solid cores are able to create almost zero birefringence as there is no asymmetry in the structure. We can see from Fig. 4 (a) that the birefringence for the rectangular core increases with wavelength. This is because, at higher wavelength the index difference between the polarization modes increases and that results high birefringence. As we mentioned earlier, the birefringence effect of a fiber makes the coupling stronger either in x polarization or y polarization that increases the sensitivity as well as the detection accuracy [38]. Note that, this is another reason of choosing the rectangular structure as the core of the proposed sensor.

Optics EXPRESS

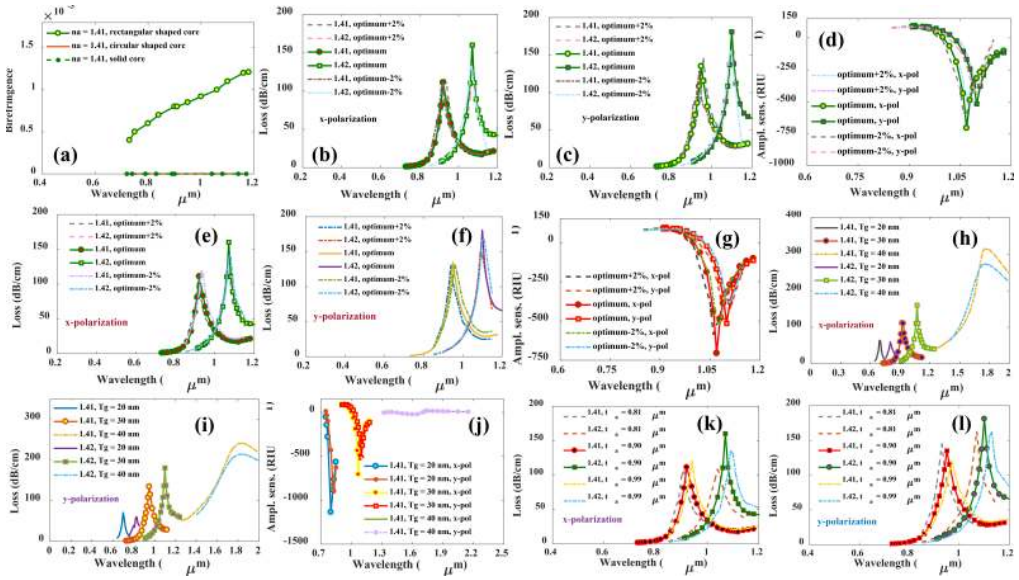

Fig. 4. Birefringence with different shaped core air hole (a), confinement loss (b-c) and amplitude sensitivity (d) at optimal d, d_1, d_2 and ±2% variation from the optimal diameters for n_a = 1.41, confinement loss (e-f) and amplitude sensitivity (g) at optimal Λ, Λ_1, Λ_2 and ±2% variation from the optimal for n_a = 1.41, confinement loss (h-i) and amplitude sensitivity (j) at different variation of gold thickness, and confinement loss (k-l) at different analyte thickness variation.

3.2. *Effect of cladding on the sensing performance*

With rectangular air hole in the core, the effect of cladding on the sensing performance including air hole diameters (d, d_1 and d_2) and pitch distances (Λ, Λ_1, and Λ_2) are investigated. This is also done to optimize the air hole diameters and pitch distances.

3.2.1. Effect of cladding air hole diameters d, d_1 and d_2

In order to choose optimum diameters of cladding air holes we varied d, d_1 and d_2 and observed the sensing performance that is shown through Fig. 4 (b-d). It indicates that changing d, d_1 and d_2 from its optimum diameter changes the loss characteristics, however the variation is not very significant. However, such variation affects the amplitude sensitivity, as shown in Fig. 4 (d). It can be seen that variation of air hole diameters from its optimum causes broadening of the loss peak and reduces amplitude sensitivity. It can be seen that a sharp loss peak and maximum sensitivity is obtained at d = 1.35 μm, d_1 = 1.20 μm, d_2 = 0.18 μm and thus we choose those values of d, d_1 and d_2 as optimum cladding air hole diameter.

3.2.2. Effect of pitch distances Λ, Λ_1, and Λ_2

The effect of pitch distances of the air holes is also investigated. Fig. 4 (e-g) shows the characteristics of the proposed sensor with different pitch variation at both x and y polarizations. From Fig. 4 (e-f) we can see that changing the pitch distances does not significantly change the confinement loss. However, comparing the loss characteristics with different pitch values we found sharper loss peak at Λ = 1.8 μm, Λ_1 = 1.6 μm, Λ_2 = 1.24 μm. As such, due to sharper loss peak, a maximum amplitude sensitivity is obtained at those values of pitch distance. Note that by varying the pitch distances, the sensor shows no significant change in wavelength sensitivity, however significant change in amplitude sensitivity is found as shown in Fig. 4 (g).

Optics EXPRESS

Thus, considering the amplitude sensitivity we choose $\Lambda = 1.8\ \mu$m, $\Lambda_1 = 1.6\ \mu$m, $\Lambda_2 = 1.24\ \mu$m as optimum pitch distances of the proposed sensor.

3.3. Effect of gold thickness on sensing performance

The thickness of the gold layer plays an important role on the sensing performance. Gold thickness also significantly affects the resonance wavelength shift. Thus the effect of gold thickness variation on the overall sensing performance is investigated. It can be seen from Fig. 4 (h-i) that as the gold thickness increases the resonance peak shifts largely towards the longer wavelengths. Moreover, it can be seen that a thicker Au layer broadens the loss peak and increases the signal to noise ratio (SNR) of the sensor.

We can see that for $t_g = 40$ nm the loss is larger, with near zero amplitude sensitivity (Fig. 4 (j)), therefore we rule out $t_g = 40$ nm as optimum. It can also be observed that, at $t_g = 20$ nm the loss is lower and the obtained amplitude sensitivity is higher than $t_g = 30$ nm. However, the obtained wavelength sensitivity at $t_g = 30$ nm is higher (15000 nm/RIU for x-pol and 15000 nm/RIU for y-pol for $n_a = 1.41$) than the obtained sensitivity at $t_g = 20$ nm (11000 nm/RIU for x-pol and 13000 nm/RIU for y-pol of $n_a = 1.41$). The sensitivity reduction for thinner gold layer is due to the skin depth limitation of the surface plasmons [3,4,31]. Moreover, making a 30 nm gold layer is easier than a 20 nm layer. Thus considering all of the above facts we choose $t_g = 30$ nm as an optimal gold thickness for the proposed sensor.

We can see from Fig. 4 (k-l) and Fig. 5 (a) that analyte thickness has significant impact on the sensor performance. It can be observed that when the channel thickness decreases to $t_a = 0.81\ \mu$m from the optimum point ($t_a = 0.9\ \mu$m) the amplitude as well as wavelength sensitivity decreases (13000 nm/RIU for x-pol and 14000 nm/RIU for y-pol of $n_a = 1.41$). The similar thing happened when we increased the channel thickness to $t_a = 0.99\ \mu$m. Therefore, considering the amplitude sensitivity, wavelength sensitivity and loss peak broadening we consider $t_a = 0.90\ \mu$m as optimum analyte thickness.

Table 2. Comparison of performance of the proposed sensor with prior sensors.

Ref.	Sensing Approach	RI Range	Birefringence	Max. Amp. Sens. (RIU^{-1})	Max. Wavel. Sens. (nm/RIU)	Sensor Resolution
[6]	External (Dual side polished)	1.23–1.29	-	333.8	5500	7.69×10^{-6}
[8]	External (Side polished)	1.33–1.35	-	74	17000	5.8×10^{-6}
[10]	External	1.33–1.37	-	860	5000	4×10^{-5}
[15]	External (Multi channel)	1.32–1.36	-	425	4600	2×10^{-5}
[21]	Internal (Multi coated)	1.45–1.49	-	–	–5500	–
[24]	Internal (selectively coated)	1.33–1.42	-	1420	11000	9.1×10^{-6}
[26]	Internal (Multi coated)	1.34–1.48	7.5×10^{-4}	–	1131	1×10^{-4}
[27]	External (Side polished)	1.345 – 1.410	–	–	12450	8.03×10^{-6}
[28]	External (Side polished)	1.28–1.34	–	178	6000	0.16×10^{-6}
[29]	External (Side polished)	1.33–1.43	-	1086	46000	2.2×10^{-6}
[32]	External (Dual side polished)	1.36–1.41	-	1222	14660	6.82×10^{-6}
[33]	External (Multi-core flat fiber)	1.46 – 1.485	-	820	23000	4.35×10^{-6}
[38]	External	1.33–1.38	-	420.4	4600	2.17×10^{-5}
[39]	External	1.40–1.43	-	498	15180	5.68×10^{-6}
This paper	External	1.33–1.43	1.2×10^{-3}	1415	62000	1.61×10^{-6}

Optics EXPRESS

3.4. Effect of PML thickness on sensing performance

Finally, we optimize the thickness of the perfectly matched layer and the characteristics are observed from Fig. 5 (b-d). The confinement loss characteristics as shown in Fig. 5(b-c) indicate that PML has very little impact on the confinement loss of the sensor. For different thickness of PML Fig. 5(d) indicate that when the PML thickness reduces to $t_p = 0.80$ μm than the optimum ($t_p = 1.0$ μm) the amplitude sensitivity greatly decreases. However, PML thickness greater than 1.0 μm produced similar sensing performance as that obtained with $t_p = 1.0$ μm. Therefore, we could choose $t_p = 1.20$ μm or more however that also increases the overall size of the sensor. Thus, considering the sensing performance and size of the sensor we choose $t_p = 1.0$ μm as optimal PML thickness.

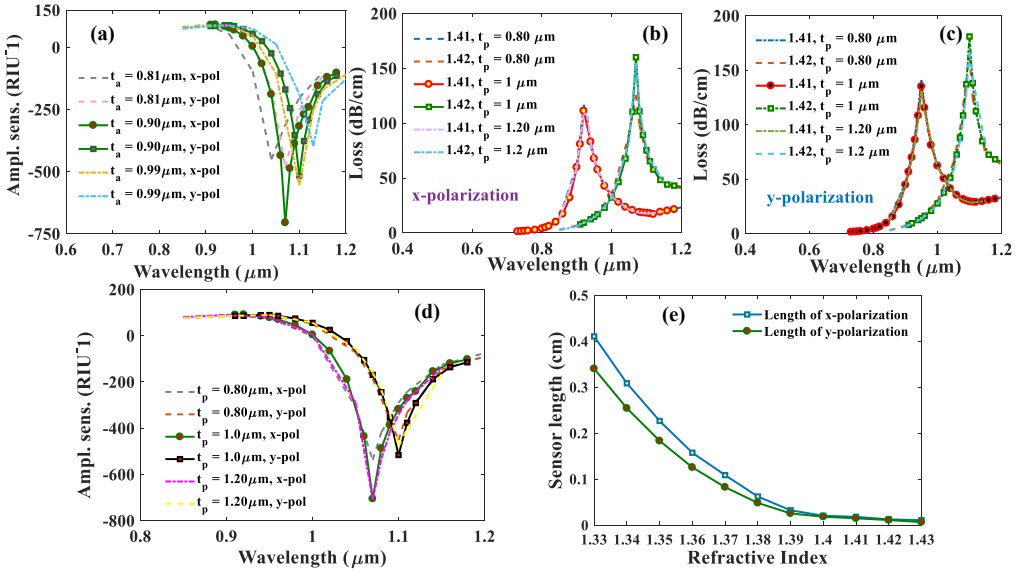

Fig. 5. Amplitude sensitivity at different analyte thickness variation (a), confinement loss (b-c) and amplitude sensitivity (d) at different variation of PML thickness, and the length of the sensor (e) at different analyte RI.

3.5. Sensor Length and Resolution Property

It is also important to investigate the length of the sensor that can be achieved using Eq. (5 (e)). As can be observed from Eq. (5 (e)) that, the length of a sensor is totally dependent on its attenuation constant. For different RI, the length of the sensor is shown in Fig. 5 (e) which indicate that the attenuation constant (α) increases with the increase of RI resulting reduction in sensor length. It can be seen that a sensor having length of centimetres to few millimetres can be used to detect analytes with different RI.

The resolution of a sensor is an important parameter by which the detection limit of the sensor can be investigated. By considering $\Delta\lambda_{\min} = 0.1$ nm, a maximum resolution of 1.72×10^{-6} and 1.61×10^{-6} is obtained for the x and y polarization, respectively. To our knowledge this is the highest resolution obtained as compared to prior reported PCF based plasmonic sensors. Note that, the resolution of the proposed sensor indicates that the sensor has the capability to detect a tiny change of RI of the order of 10^{-6}. Therefore, the proposed sensor can effectively be used to detect the tiny change of analyte RI.

A performance analysis of the proposed PCF-SPR sensor with the prior sensors is carried out in Table 3.3. Based on the performance analysis of wavelength sensitivity, amplitude sensitivity,

sensor resolution and birefringence it can be seen that the proposed sensor shows improved performance over the prior sensors presented in the literature. Moreover, due to practical sensing approach, the proposed sensor increases its potential for further real time measurements of analytes.

4. Conclusions

A novel PCF based SPR sensor has been designed and characterized for optical detection of biological, biochemical and biomedical analytes. Detailed numerical simulation and extensive analysis of the sensor shows a maximum wavelength sensitivity of 58000 nm/RIU for x polarization and 62000 nm/RIU for y polarization, maximum amplitude sensitivity of 1415 RIU^{-1} for x polarization and 1293 RIU^{-1} for y polarization respectively within the analyte RI of 1.33 to 1.43. Moreover, the sensor can achieve a maximum birefringence of 1.2×10^{-3} that facilitates the fiber to be operated in a dual polarized mode and improves the sensing performance. The sensor also shows a maximum resolution of 1.72×10^{-6} and 1.6×10^{-6} for the x and y polarization respectively. Moreover, the sensor achieves a maximum FOM of 1140 for the x polarization and 958 for the y polarization that validates the performance improvement of it. To our knowledge the obtained sensitivity and sensor resolution is better than any prior reported PCF-SPR sensors. The fabrication of the sensor is straightforward with existing technologies. The practical utilization is simple as it uses an external sensing approach. With such remarkable sensing properties the proposed sensor shows great potential in the field of biomedicine, chemistry and for accurate and precise detection of other biological and biomedical agents.

Funding

Australian Research Council (ARC) (DP170104984).

Acknowledgments

This work is supported by Australian Research Council (grant no. DP170104984). We gratefully acknowledge their support.

References

1. E. Kretchmann and Z. H. Raether, "Radiative decay of non radiative surface plasmon excited by light," Z. Naturforsch. A. Phys. Sci. **23**, 2135–2136, (1968).
2. L. G. Carrascosa, "Molecular inversion probe-based SPR biosensing for specific, label-free and real-time detection of regional DNA methylation," Chem. Commun. **50**(27), 3585–3588, (2014).
3. J. Homola, S. S. Yee, and G. Gauglitz, "Surface plasmon resonance sensors: review," Sens. & Actuators B **54**, 3–15, (1999).
4. J. Homola,"Present and future of surface plasmon resonance biosensors," Anal. Bioanal. Chem. **377**, 528–539, (2003).
5. B. Lee, S. Roh, J. Park, "Current status of micro and nano-structured optical fiber sensors," Optical Fiber Technol. **15**, 209–221, (2009).
6. C. Liu, L. Yang, X. Lu, Q. Liu, F. Wang, J. Lv, T. Sun, H. Mu, and P. K. Chu, "Mid-infrared surface plasmon resonance sensor based on photonic crystal fibers," Opt. Exp. **25**(13), 14227–14237, (2017).
7. G. Robinson, "The commercial development of planar optical biosensors," Sens. Actuators B Chem. **29**(1), 31–36, (1995).
8. J. N. Dash, R. Jha, "Highly sensitive side-polished birefringent PCF-based SPR sensor in near IR," Plasmonics **11**(6), 1505–1509, (2016).
9. R. Jha and G. Badenes, "Effect of fiber core dopant concentration on the performance of surface plasmon resonance-based fiber optic sensor," Sensor. Actuat. A-Phys. **150**(2), 212–217, (2009).
10. J. N. Dash and R. Jha,"Graphene based birefringent photonic crystal fiber sensor using surface plasmon resonance," IEEE Photonics Technol. Lett. **26**(11), 1092–1095, (2014).
11. C. Caucheteur, T. Guo, and J. Albert,"Review of plasmonic fiber optic biochemical sensors: improving the limit of detection," Anal. Bioanal. Chem. **407**(14), 3883–3897, (2015).
12. A. Hassani and M. Skorobogatiy, "Design of the microstructured optical fiber-based surface plasmon resonance sensors with enhanced microfluidics," Opt. Exp. **14**(24), 11616–11621, (2006).

13. J. Yao, X. Yang, M. Wang, and Y. Lu,"Surface plasmon resonance sensor based on hollow-core PCFs filled with silver nanowires," Electron. Lett. **51**(21), 1675–1677, (2015).
14. A. A. Rifat, G. Mahdiraji, D. Chow, Y. Shee, R. Ahmed, F. Adikan, "Photonic crystal fiber-based surface plasmon resonance sensor with selective analyte channels and graphene-silver deposited core," Sensors **15**(5), 11499–11510, (2015).
15. R. Otupiri, E. Akowuah, S. Haxha,"Multi-channel SPR biosensor based on PCF for multi-analyte sensing applications," Opt. Exp. **23**(12), 15716–15727, (2015).
16. Y. Peng, J. Hou, Y. Zhang, Z. Huang, R. Xiao, and Q. Lu,"Temperature sensing using the bandgap-like effect in a selectively liquid-filled photonic crystal fiber," Opt. Lett. **38**(3), 263–265, (2013).
17. J. Xue, S. Li, Y. Xiao, W. Qin, X. Xin, and X. Zhu, "Polarization filter characters of the gold-coated and the liquid filled photonic crystal fiber based on surface plasmon resonance, " Opt. Exp. **21**(11), 13733–13740, (2013).
18. R. Zakaria, W. Kam, Y. S. Ong, S. F. A. Z. Yusoff, H. Ahmad and Waleed S. Mohammed, "Fabrication and simulation studies on D-shaped optical fiber sensor via surface plasmon resonance, " Journal of Modern Optics **64**(14), 1443–1449, (2017).
19. W. Qin, S. Li, Y. Yao, X. Xin, and J. Xue, "Analyte-filled core self-calibration microstructured optical fiber based plasmonic sensor for detecting high refractive index aqueous analyte, " Optics and Lasers in Engineering **58**(14), 1–8, (2014).
20. A. Khaleque and H. T. Hattori, "Polarizer based upon a plasmonic resonant thin layer on a squeezed photonic crystal fiber, " Appl. Opt. **54**(9), 2543–2549, (2015).
21. B. Shuai, L. Xia, and D. Liu,"Coexistence of positive and negative refractive index sensitivity in the liquid-core photonic crystal fiber based plasmonic sensor, " Opt. Exp. **20**(23), 25858–25866, (2012).
22. L. Duan, X. Yang, Y. Lu, and J. Yao, "Hollow-fiber-based surface plasmon resonance sensor with large refractive index detection range and high linearity, " Appl. Opt. **56**(36), 9907–9912, (2017).
23. B. Shuai, L. Xia, Y. Zhang, and D. Liu, "A multi-core holey fiber based plasmonic sensor with large detection range and high linearity, " Opt. Exp. **20**(6), 5974–5986, (2012).
24. A. A. Rifat, F. haider, R. Ahmed, G. A. Mahdiraji, F. R. M. Adikan, and A. E. Miroshnichenko, "Highly sensitive selectively coated photonic crystal fiber-based plasmonic sensor, " Opt. Lett. **43**(4), 891–894, (2018).
25. N. Luan, R. Wang, W. Lv, and J. Yao, "Surface plasmon resonance sensor based on D-shaped microstructured optical fiber with hollow core," Opt. Exp. **23**(7), 8576–8582, (2015).
26. C. Liu, F. Wang, S. Zheng, T. Sun, J. Lv, Q. Liu, L. Yang, H. Mu & P. K. Chu, "Analysis of a highly birefringent asymmetric photonic crystal fibre based on a surface plasmon resonance sensor," Journal of Modern Optics **63**(12), 1189–1195, (2016).
27. G. Wang, S. Li, G. An, X. Wang, Y.Zhao, W. Zhang, & H. Chen, "Highly sensitive D-shaped photonic crystal fiber biological sensors based on surface plasmon resonance," Optical and Quantum Electronics **48**(46), (2016).
28. T. Huang, "Highly sensitive SPR sensor based on D-shaped photonic crystal fiber coated with Indium Tin Oxide at near-infrared wavelength," Plasmonics **12**(3), (2017).
29. A. A. Rifat, R. Ahmed, G. A. Mahdiraji and F. R. M. Adikan, "Highly sensitive D-shaped photonic crystal fiber-based plasmonic biosensor in visible to near-IR," IEEE Sensors Journal **17**(9), 2776–2783, (2017).
30. Q. Xie, Y. Chen, X. Li, Z. Yin, L. Wang, Y. Geng, and X. Hong, "Characteristics of D-shaped photonic crystal fiber surface plasmon resonance sensors with different side-polished lengths," Appl. Opt. **56**(5), 1550–1555, (2017).
31. G. An, X. Hao, S. Li, X. Yan, and X. Zhang, "D-shaped photonic crystal fiber refractive index sensor based on surface plasmon resonance," Appl. Opt. **56**(24), 6988–6992, (2017).
32. C. Liu, W. Su, Q. Liu, X. Lu, F. Wang, T. Sun, and P. K. Chu, "Symmetrical dual D-shape photonic crystal fibers for surface plasmon resonance sensing, " Opt. Exp. **26**(7), 9039–9049, (2018).
33. A. A. Rifat, G. A. Mahdiraji, Y. M. Sua, R. Ahmed, Y. G. Shee, and F. R. Mahamd Adikan, "Highly sensitive multi-core flat fiber surface plasmon resonance refractive index sensor, " Opt. Exp., **24**(3) 2485–2495, (2016).
34. J. N. Dash and R. Jha, "On the performance of graphene-based D-shaped photonic crystal fibre biosensor using surface plasmon resonance," Plasmonics **10**(5), 1123–1131, (2015).
35. R. Otupiri, E. K. Akowuah, S. Haxha, H. Ademgil, F. AbdelMalek and A. Aggoun, "A novel birefrigent photonic crystal fiber surface plasmon resonance biosensor," IEEE Photonics Journal **6**(4), 1–11, (2014).
36. A. A. Rifat, G. A. Mahdiraji, Y. M. Sua, Y. G. Shee, R. Ahmed, D. M. Chow and F. R. Mahamd Adikan, "Surface plasmon resonance photonic crystal fiber biosensor: A practical sensing approach," IEEE Photonics Technol. Lett. **27**27(15), 1628–1831, (2015).
37. A. A. Rifat, G. A. Mahdiraji, R. Ahmed, D. M. Chow, Y. M. Sua, Y. G. Shee, and F. R. Mahamd Adikan, "Copper-graphene-based photonic crystal fiber plasmonic biosensor," IEEE Photonics Journal **8**(1), 1–8, (2016).
38. M. R. Hasan, S. Akter, A. A. Rifat, S. Rana, K. Ahmed, R. Ahmed, H. Subbaraman, D. Abbott "Spiral photonic crystal fiber-based dual-polarized surface plasmon resonance biosensor," IEEE Sensors Journal **18**(1), 133–140, (2018).
39. M. Liu, X. Yang, P. Shum, and H. Yuan, "High-sensitivity birefringent and single-layer coating photonic crystal fiber biosensor based on surface plasmon resonance, " Appl. Opt. **57**(8), 1883–1886, (2018).
40. R. Ziblat, V. Lirtsman, D. Davidov, B. Aroeti, "Infrared surface plasmon resonance: A novel tool for real time sensing of variations in living cells, " Biophys. J. **90**(7), 2592–2599, (2006).
41. L. Peng, F. Shi, G. Zhou, S. Ge, Z. Hou and C. Xia, "A surface plasmon biosensor based on a D-shaped microstructured optical fiber with rectangular lattice, " IEEE Photonics Journal **7**(5), 1–9, (2015).

Optics EXPRESS

42. P. J. A. Sazio, A. Amezcua-Correa, C. E. Finlayson, J. R. Hayes, T. J. Scheidemantel, N. F. Baril, B. R. Jackson, D.-J. Won, F. Zhang, E. R. Margine, V. Gopalan, V. H. Crespi, and J. V. Badding, "Microstructured optical fibers as high-pressure microfluidic reactors, " Science **311**(5767), 1583–1586, (2006).
43. I. H. Malitson, "Interspecimen comparison of the refractive index of fused silica, " J. Opt. Soc. Am. **55**(10), 1205–1208, (1695).
44. A. Vial, A.-S. Grimault, D. Macas, D. Barchiesi, and M. L. de La Chapelle, "Improved analytical fit of gold dispersion: application to the modeling of extinction spectra with a finite-difference time-domain method, " Phys. Rev. B **71**(085416), (2005).
45. B. Gauvreau A. Hassani M. Fassi Fehri A. Kabashin M. A. Skorobogatiy, "Photonic bandgap fiber-based surface plasmon resonance sensors, " Opt. Exp. **15**(18), 11413–11426, (2007).
46. M. S. Islam, J. Sultana, K. Ahmed, A. Dinovitser, M. R. Islam, B. W.-H. Ng and D. Abbott "A novel approach for spectroscopic chemical identification using photonic crystal fiber in the terahertz regime," IEEE Sensors Journal **18**(2), 575–582, (2018).
47. M. S. Islam, J. Sultana, A. A. Rifat, A. Dinovitser, B. W.-H. Ng and D. Abbott "Terahertz sensing in a hollow core photonic crystal fiber ," IEEE Sensors Journal **18**(10), 4073–4080, (2018).
48. M. Hautakorpi, M. Mattinen, and H. Ludvigsen, "Surface-plasmon-resonance sensor based on three-hole microstructured optical fiber, " Opt. Exp. **16**(12), 8427–8432, (2008).
49. G. A. Mahdiraji, D. M. Chow, S. R. Sandoghchi, F. Amirkhan, E. Dermosesian, K. S. Yeo, Z. Kakaei, M. Ghomeishi, S. Y. Poh, S. Y. Gang & F. R. M. Adikan "Challenges and solutions in fabrication of silica-based photonic crystal fibers: An experimental study, " Fiber Integr. Opt. **33**(1), 85–104, (2014).
50. J. C. Knight "Photonic crystal fibers," Nature. **424**, 847–851, (2003).
51. S. Atakaramians, S. Afshar, H. Ebendorff Heidepriem, M. Nagel, B. M. Fischer, D. Abbott, and T. M. Monro, "THz porous fibers: design, fabrication and experimental characterization," Opt. Exp. **17**(16), 14053–14062, (2009).
52. S. Atakaramians "Terahertz waveguides: A study of microwires and porous fibre " PhD thesis, , The University of Adelaide, 146–156, (2011). Available: https://digital.library.adelaide.edu.au/dspace/handle/2440/69317.
53. H. Ebendorff-Heidepriem, J. Schuppich, A. Dowler, L. Lima-Marques, and T. Monro, "3D-printed extrusion dies: A versatile approach to optical material processing," Opt. Mater. Express **4**(8), 1494–1504, (2014).
54. C. R. Kurkjian, J. T. Krause and M. J. Matthewson, "Strength and fatigue of silica optical fibers," Journal of Lightwave Technol. **7**(9), 1360–1370, (1989).
55. M. Bayindir, F. Sorin, A. F. Abouraddy, J. Viens, S. D. Hart, J. D. Joannopoulos & Y. Fink "Metal insulator-semiconductor optoelectronic fibres," Nature **431**, 826–829, (2004).
56. P. J. A. Sazio, A. Amezcua-Correa, and C. E. Finlayson, "Microstructured optical fibers as high-pressure microfluidic reactors," Science **311**, 1583–1586, (2006).
57. X. Zhang, R. Wang, F. M. Cox, B. T. Kuhulmey, and M. C. J. Large, "Selective coating of holes in microstructured optical fiber and its application to in-fiber absorptive polarizers," Opt. Exp. **15**(24), 16270–16278, (2007).
58. Y. Peng, J. Hou, Y. Zhang, Z. Huang, R. Xiao, & Q. Lu, "Temperature sensing using the bandgap-like effect in a selectively liquid-filled photonic crystal fiber," Opt. Lett. **38**(3), 263–265, (2013).
59. T. Srivastava, R. Das, & R. Jha "Highly sensitive plasmonic temperature sensor based on photonic crystal surface plasmon waveguide," Opt. Lett. **8**(2), 515–521, (2013).
60. A. Aray, F. Chiavaioli, M. Arjmand, C. Trono, S. Tombelli, A. Giannetti, N. Cennamo, M. Soltanolkotabi, L. Zeni, and F. Baldini, "SPR-based plastic optical fibre biosensor for the detection of C-reactive protein in serum," J. Biophoton. **9**(10), 1077–1084, (2016).
61. A. K. Yetisen, H. Butt, T. Mikulchyk, R. Ahmed, Y. Montelongo, M. Humar, N. Jiang, S. Martin, I. Naydenova, and S. H. Yun, "Color-selective 2.5D holograms on large-area flexible substrates for sensing and multilevel security," Adv. Opt. Mat. **4**(10), 1589–1600, (2016).